ROYAL SOCIETY OPEN SCIENCE

rsos.royalsocietypublishing.org

Research

Cite this article: Liu X, Fan H-Q. 2018 Electronic structure, elasticity, Debye temperature and anisotropy of cubic WO_3 from first-principles calculation. *R. Soc. open sci.* **5**: 171921. http://dx.doi.org/10.1098/rsos.171921

Received: 15 November 2017
Accepted: 14 May 2018

Subject Category:
Chemistry

Subject Areas:
molecular computing/atomic and molecular physics/quantum physics

Keywords:
first principle, electronic structure, elastic properties, Debye temperature, acoustic wave velocity, cubic WO_3

Author for correspondence:
Hui-Qing Fan
e-mail: hqfan3@163.com

This article has been edited by the Royal Society of Chemistry, including the commissioning, peer review process and editorial aspects up to the point of acceptance.

Electronic supplementary material is available online at https://dx.doi.org/10.6084/m9.figshare.c.4117070.

THE ROYAL SOCIETY PUBLISHING

Electronic structure, elasticity, Debye temperature and anisotropy of cubic WO_3 from first-principles calculation

Xing Liu and Hui-Qing Fan

State Key Laboratory of Solidification Processing, School of Materials Science and Engineering, Northwestern Polytechnical University, Xi'an 710072, People's Republic of China

XL, 0000-0001-6897-5523

The electron structure, elastic constant, Debye temperature and anisotropy of elastic wave velocity for cubic WO_3 are studied using CASTEP based on density functional theory. The optimized structure is consistent with previous work and the band gap is obtained by computing the electronic structure; the top of the valence band is not at the same point as the bottom of the conduction band, which is an indirect band-gap oxide. Electronic properties are studied from the calculation of band structure, densities of states and charge densities. The bulk and shear moduli, Young's modulus, hardness and Poisson's ratio for WO_3 are studied by the elastic constants. We calculated acoustic wave velocities in different directions and estimated the Debye temperature from the acoustic velocity. The anisotropy of WO_3 was analysed from the point of view of a pure wave and quasi wave.

1. Introduction

As a type of excellent semiconductor material, tungsten trioxide (WO_3) has been widely used in multiphase catalysis, electroluminescence, photodegradation, high-temperature superconductivity and new energy fields [1–10]. The ideal cubic WO_3 primitive cell is a kind of octahedral structure; W and O occupy the central and six corners of the octahedron (figure 1), respectively.

Tungsten trioxide experiences different structure transitions in the temperature range of −180 to 900°C; these phase transitions are not the recombination of tungsten and oxygen atoms, but the distortion of tungsten atoms in the original ideal

© 2018 The Authors. Published by the Royal Society under the terms of the Creative Commons Attribution License http://creativecommons.org/licenses/by/4.0/, which permits unrestricted use, provided the original author and source are credited.

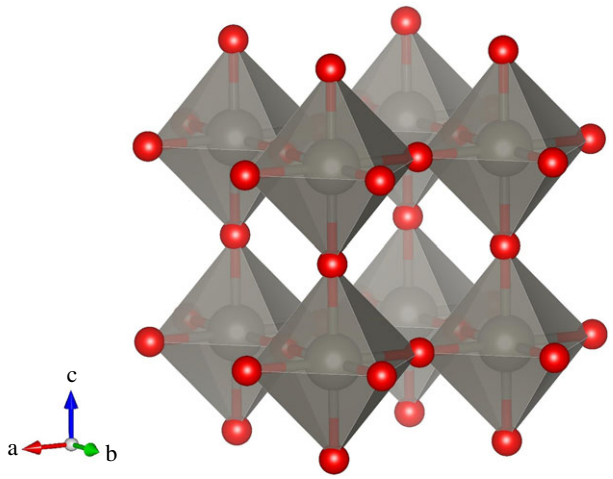

Figure 1. Crystal structure of cubic WO_3. There are four atoms in the WO_3 primitive cell: three O atoms at (0, 0, 0), (0, a/2, a/2) and (a/2, 0, a/2) and one W (0, 0, a/2), where a is the lattice constant.

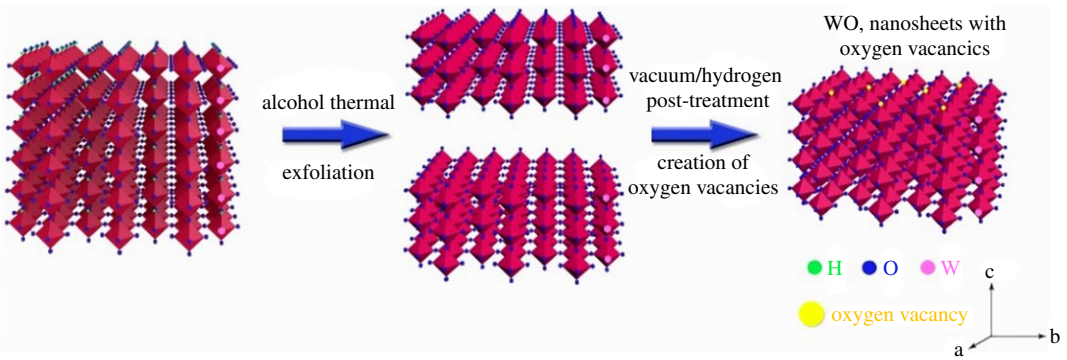

Figure 2. Schematic illustration describing the formation of tungsten oxide single crystal nanosheets [23].

crystal structure. The phase transition, from low to high temperature; is irreversible; a stable phase that forms at high temperature is also stable at low temperatures. As the temperature increases, the sequence of WO_3 phase transitions is as follows: monoclinic (at low temperature) → triclinic → monocline (at room temperature) → orthorhombic phase → tetragonal phase. Of course, there is also hexagonal phase WO_3. Although cubic WO_3 has not been observed at high temperatures, in many works it is considered as a reference structure, with many reports on experimental and theoretical studies of WO_3.

Since the 1970s, when Randin [11] found tungsten oxide with photochromic performance for the first time, many research works both at home and abroad have conducted a number of theoretical and experimental studies on photocatalysis, capacitance performance, photosensitivity and gas sensitivity of tungsten oxide [12–21]. Yan *et al*. [22] published an article on hydrogenation of WO_3. They synthesized tungsten oxide single-crystal nanosheets via the exfoliation of layered tungstic acid to tungsten oxide nanosheets and subsequent introduction of oxygen vacancies (figure 2). In Taiwan, Hsieh *et al*. [23] studied the growth along the [001] direction of triclinic WO_3 nanowires, and the optical absorption of nanowires by the red shift phenomenon. The results showed the influence of oxygen vacancy on the red shift, and the influence of crystallinity and particle size distribution of the nanowires on the forbidden bandwidth. Hao Lai *et al.* [24] fabricated mesoporous WO_3 nanofibres and tube-like nanofibres by the gas-filled assistant sol–gel immersion method with porous anodic alumina membrane confinement, which has a porous structure (figure 3). Wang *et al*. [25] studied the structural and electronic properties of WO_3 by various hybrid functionals combined with both plane wave and localized basis sets. Levy & Pagnier [26], through the establishment of sheet WO_3 to simulate a nanoscale with the required stoichiometric ratio and oxygen-containing defects, computed the position of the atoms, electron density and the electron state density distribution, and pointed out that the WO_3 surface could absorb oxygen

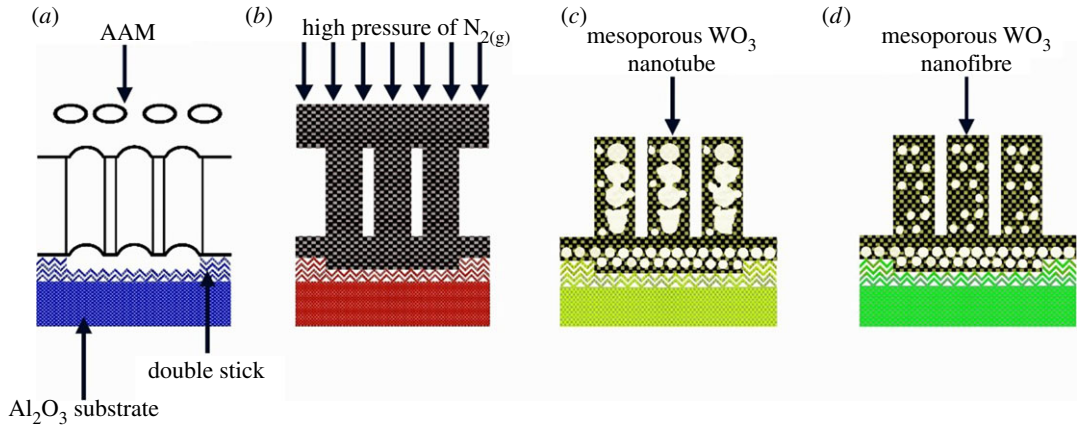

Figure 3. Gas-filled process of mesoporous tungsten oxide nanowire synthesis from triblock co-polymer within a porous anodic alumina membrane (AAM) [25].

atoms, which is due to the existence of the acceptor level at the bottom of the surface valence band. Chatten *et al*. [27] studied the WO_3 electron structure of the oxygen vacancy model in different crystal systems and its forbidden band gap, and found that the polarizations of the bonding and anti-bonding states were not only related to the location of the crystal system but also to the position of oxygen vacancy.

By reviewing the previous work, it has been found that the study of tungsten oxide experimentally and theoretically has made great advancements, but systematic studies of its elastic properties, Debye temperature and anisotropy are rare. It is well known that elastic properties can be used to provide information about the potential of atoms and relate to a variety of basic solid-state phenomena. Therefore, this paper is based on density functional theory (DFT) to study the cubic WO_3 electronic structure, elastic properties, Debye temperature and anisotropy in different directions.

2. Computational details

In recent years, the methods used for theoretical study of metal oxides have been mainly based on LDA, GGA, LDA + U and GGA + U [28–34]; Hubbard parameter U is known as the On-site Coulomb interaction energy [35]. However, a strong association effect is not considered in the calculation of LDA and GGA, that is, the unoccupied d and f orbits. Furthermore, because of the complexity of the electron cloud diffusion, the multibody effect of an orbit is difficult to accurately describe by LDA and GGA. In this system, the energy band structure of the metal is often given by LDA or GGA, and the bands across the Fermi level are often d or f orbits. In fact, the band structure of the system has semiconductor characteristics, there is a clear band gap between the bonding and the anti-bonding states, and the d or f orbit is tightly confined to the nucleus and does not show delocalization. To better describe the strong association system, it is necessary to surpass the traditional LDA or GGA approximation. In this respect, the more successful methods of improvement are LDA + U and GGA + U. Compared with the traditional DFT, the calculation of LDA(GGA) + U does not increase obviously, and the calculation results can be improved significantly with the proper parameters.

In this work, we use DFT to study electronic structure, elastic properties, Debye temperature and anisotropy of cubic WO_3; the calculations have been performed by the CASTEP code [36,37]. By comparison of different approximation methods, LDA + U [38] is finally determined for structural optimization. W $5d^4 6s^2$ electrons and O $2s^2 2p^4$ electrons are explicitly treated as valence electrons. According to the results of the convergence (figure 4), the cut-off energy of the plane wave is taken as $E_{cut} = 700$ eV, the *k*-point integral in the Brillouin zone is set to $7 \times 7 \times 7$ and the self-consistent convergence method is used to optimize the structure of cubic WO_3.

3. Results and discussion

We optimized at the LDA + U (U = 5 eV [35]) level the lattice constant of the cubic WO_3 to be 3.82 Å, which agrees quite well with those of previous self-consistent calculations: $a = 3.73$–3.84 Å [39–41], as well as the experimental value of $a = 3.71$–3.75 Å [42]. Optimized results by GGA + U are larger than

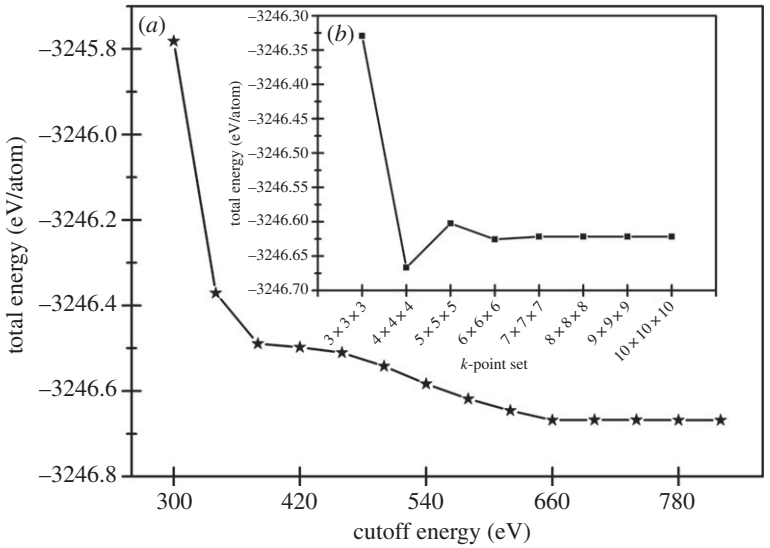

Figure 4. Convergences of the total energy of WO_3 at different computational parameters. (*a*) Total energy versus the cut-off energy for the *k*-point of 4 × 4 × 4. (*b*) Total energy versus the *k*-point for the cut-off energy of 700 eV.

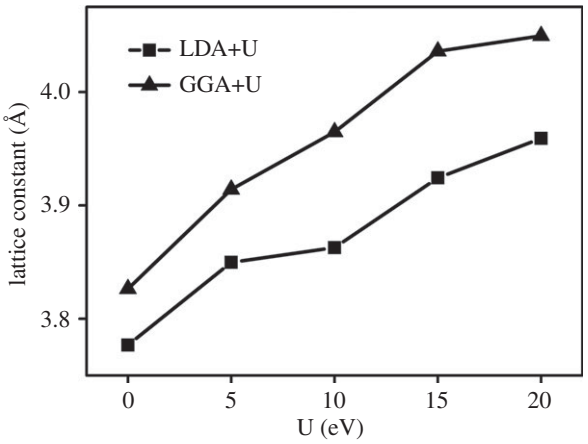

Figure 5. Optimized lattice constant of WO_3. U values are specified where applicable.

those of the above theoretical and experimental studies (figure 5), which indicates that LDA + U is more suitable for structural optimization than GGA + U in this work.

3.1. Electronic structure

The calculated band gap, $E_g = 0.544$ eV, is in line with the previous theoretical studies, $E_g = 0.3$–0.6 eV [43,44], which is much smaller than the experimental value of 2.62 eV (for the monoclinic phase) [45] due to the well-known DFT error. The results can be modified by using the scissors operator [46], and the band-gap width of WO_3 is $E_g = 2.70$ eV, which does not affect our next step of calculation.

As shown in figure 6, the WO_3 band gap can attain the maximum value at the R point (the top of the valence band) and the minimum value at the G point (bottom of the conduction band), so WO_3 is an indirect band-gap semiconductor. The valence band consists of 12 levels, which can be divided into four bands: three bonding and one non-bonding bands of hybridized O-2s, -2p and W-5d, -6s states. Based on the crystalline field theory, it can be seen that the lowest three states form a_{1g}, which is mainly due to the hybridization of the O-2s orbitals with a few of W 5d(x^2–y^2) and 5d(z^2). Three states of e_g are formed by the hybrids of W-5d(z^2) and 5d(x^2–y^2) with O-2p orbitals. The energy of e_g is lower than that of the t_{2g} band, because the overlap of the d orbitals with O-2p orbitals is stronger than that of the t_{2g}band, which is generated by the interaction between W-5d (d_{xy}, d_{xz}, d_{yz}) and O-2p orbitals. Three levels near the top of

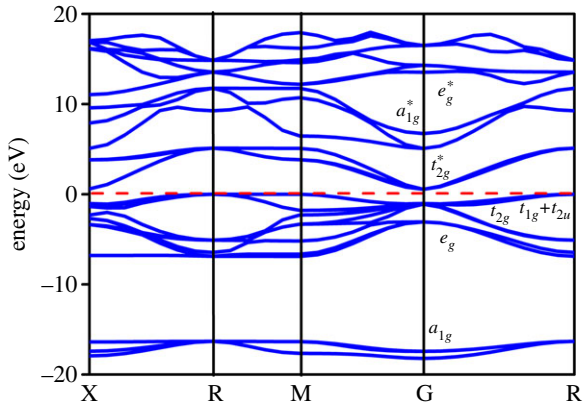

Figure 6. Band structure of WO_3. The red dashed line represents the Fermi energy level.

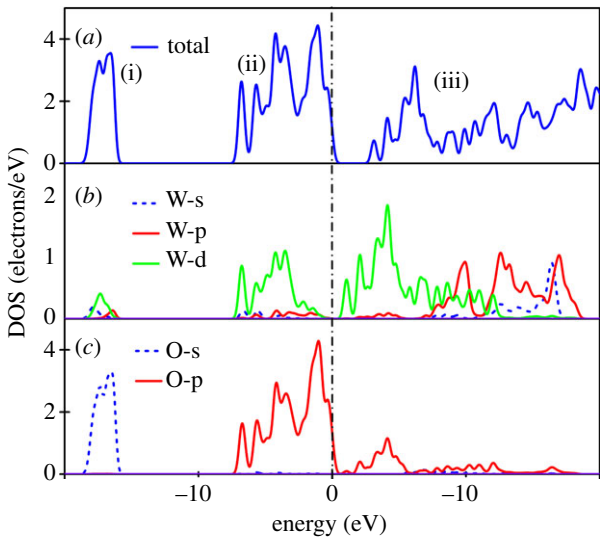

Figure 7. (*a-c*) The total and partial density of state for cubic WO_3.

the valence band form the $t_{1g} + t_{2u}$ non-bonding band; the formations are due to the interaction between the nearest O–O. In the conduction band, the energy of t_{2g}^* (anti-bonding band) is lower than that of e_g^* (anti-bonding band). It is worth noting that the a_{1g}^* anti-bonding band is between t_{2g}^* and e_g^*.

As can be seen in figure 7, the calculated density of states (DOS) of WO_3 is divided into three groups. The low-valence band (i), that is, with a bandwidth of 2.93 eV, is mainly composed of O-2s, and a minority of W-5d. Group (ii), near the top of the valence band, with a bandwidth of 7.63 eV, is formed by hybridization between O-2p and W-5d, and the contribution of tiny amounts of W-5p, -6 s. Group (iii) is located in the conduction band with a bandwidth of 13.87 eV. In the bottom of the conduction band, we found that there is a mixture of dominant O-2p with W-5d t_{2g}^* orbitals, and in the upper area of group (iii), the main contribution is by hybridization between W-5p and -6s electrons. The electronegativity for W (1.7) and O (3.44) has a small difference; consequently, hybridized peaks are dispersive and intensities are not strong enough, which is also the cause of WO_3 instability. Furthermore, the total charge densities of cubic WO_3 is presented in figure 8; it shows that the bonds between W and O are covalent due to hybridization, which agrees well with our analysis of DOS.

3.2. Elastic and mechanical properties

According to Hooke's law, there are only three independent elastic constants C_{11}, C_{12} and C_{44} for cubic crystal structures ($C_{11} = C_{22} = C_{33}$, $C_{12} = C_{13} = C_{23}$, $C_{44} = C_{55} = C_{66}$). Here. $C_{11} = 546$, $C_{12} = 35$ and

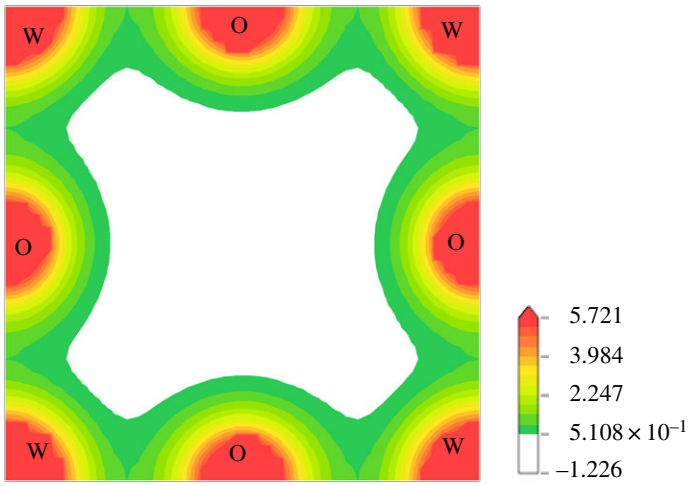

Figure 8. Charge densities of cubic WO_3.

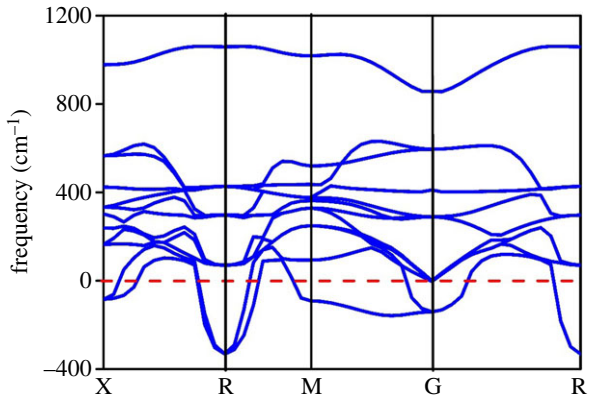

Figure 9. Phonon dispersion diagram for WO_3.

$C_{44} = 71$. Based on the Born's stability restrictions [47]:

$$C_{11} > 0, \quad C_{44} > 0, \quad C_{11} > |C_{12}|, \quad (C_{11} + 2C_{12}) > 0. \tag{3.1}$$

It is known that the elastic constants of the cubic WO_3 are satisfied with the above stability conditions, so the cubic WO_3 is stable in mechanics.

We further calculated the phonon dispersion of WO_3, whose imaginary frequency can be found from figure 9, which indicates that the cubic WO_3 structure is unstable, which is not a contradiction with the above equation (3.1). In cubic WO_3, the obtained results by the Born's stability restrictions show that the stability is affected by the external force, that is, from the point of view of macroscopic mechanics. While the imaginary frequency of the phonon dispersion shows that the atomic arrangement is unstable at present, from the point of view of microscopic atomic structure, atoms in the WO_3 will be rearranged by the lattice vibration to form a new and stable structure.

The bulk and shear modulus are two key parameters for the characterization of material hardness. The bulk modulus can be described as the ability of the material to resist the change of bulk, and is also understood as the mean value of the bond strength. The shear modulus can be described as the ability of the material to resist the shape change caused by shear force, and the ability to resist the change of the bond angle. The calculation of the bulk and shear modulus can be obtained by C_{ij}, and there are two different methods to do so. One is the calculation of the strain continuity on grain boundaries by Reuss [48], and another is Voigt's [49] proposed stress continuity on the grain boundary. Hill [50] proves that the calculations of the Reuss and Voigt models are the lower and upper limit of the elastic constants, respectively, so the Hill model calculates the arithmetic mean of the results of the Reuss and the Voigt

Table 1. According to equations (3.2)–(3.6), the bulk modulus, shear modulus and Young's modulus of WO_3 are calculated.

bulk modulus			shear modulus		
B_V	B_R	B_H	G_V	G_R	G_H
205	205	205	145	100	123
228(DFT), 225(ABOP) [51]; 224(DFT) [44]; 151 [52]; 254 [53]			123(DFT) [55]		
Young's modulus			**Pugh**		
E_V	E_R	E_H	B_V/G_V	B_R/G_R	B_H/G_H
352	258	305	1.41	2.05	1.67
311(DFT) [54]					

models:

$$B_{\mathrm{Hill}} = \tfrac{1}{2}(B_{\mathrm{Reuss}} + B_{\mathrm{Voigt}}); \quad G_{\mathrm{Hill}} = \tfrac{1}{2}(G_{\mathrm{Reuss}} + G_{\mathrm{Voigt}}), \tag{3.2}$$

where

$$B_R = B_V = \tfrac{1}{3}(C_{11} + 2C_{12}), \tag{3.3}$$

$$G_V = \tfrac{1}{5}(C_{11} - C_{12} + 3C_{44}) \tag{3.4}$$

and

$$G_R = \frac{5(C_{11} - C_{12})C_{44}}{4C_{44} + 3(C_{11} - C_{12})}. \tag{3.5}$$

The Young's modulus E of cubic crystal material can be expressed as the corresponding coefficient:

$$E = \frac{9B_xG_x}{G_x + 3B_x}, \tag{3.6}$$

where x represents Reuss, Voigt and Hill.

The comparison of our calculated data and available theoretical studies [51–54] has been presented in table 1. It is obvious that our calculation constants are in accordance with previous work. According to the criterion of Pugh [55], B_X/G_X, which is defined as the shear modulus corresponding to the plastic deformation, and the bulk modulus are related to the fracture resistance. Pugh proposed that if B_X/G_X exceeds the critical value (1.75), the material will have ductility. In our calculation, the value is less than 1.75, which indicates that cubic WO_3 has little ductility, which is also explained in the next study on Poisson's ratio.

Hence, we introduced the study of the Vickers hardness, which is an empirical formula for evaluating the hardness of the material.

$$H_V = 2(k^2G)^{0.585} - 3 \tag{3.7}$$

and

$$\upsilon = \frac{1}{2}\frac{B_x - (2/3)G_x}{B_x + (1/3)G_x}, \tag{3.8}$$

where k is the Pugh ratio, which is the ratio of the shear G to the bulk B modulus, $k = G/B$.

Compared to other metal oxides in table 2, we can see that WO_3 has greater hardness. This is due to the fact that the bulk modulus is not directly related to the hardness, and the shear modulus is more capable of characterizing the hardness of the material. Furthermore, with regard to the Poisson ratio, it reflects the strength of the covalent bond in the material. In general, the Poisson ratio $0.1 \sim 0.28$ represents the covalent property of the material, while $0.29 \sim 0.33$ represents the metal characteristics. The Poisson ratios for the above metal oxides, except for WO_3 and MgO, are more than 0.29, which means that they have metal properties along with their mechanical properties, and their hardness is less than that of WO_3.

3.3. Debye temperature

Debye temperature is a very important thermodynamic parameter reflecting thermodynamic properties, which is related to many physical properties of solids, such as acoustic velocity, specific heat capacity and thermal expansion coefficient. According to the above bulk and shear modulus, we calculated wave velocity v_s, longitudinal wave velocity v_p and average wave velocity v_m, and further studied the Debye

Table 2. Vickers' hardness and Poisson's ratio for WO_3 compared to the other calculated results.

	B	G	H_V	υ
WO_3	205	123	15.3	0.252
ZrO_2 [56]	196	92	8.62	0.297
HfO_2 [57]	293	103	5.85	0.342
TiO_2 [58]	174	70	5.27	0.363
CaO [59]	144	88	12.4	0.266
MgO [60]	139	114	22.3	0.178

Table 3. Calculation of the elastic shear wave velocity v_s, longitudinal wave velocity v_p, average wave velocity v_m and the Debye temperature of WO_3.

υ_s^X			υ_p^X		
$X = V$	$X = R$	$X = H$	$X = V$	$X = R$	$X = H$
4659	3869	4291	7722	7117	7432
υ_m^X			Θ^X		
$X = V$	$X = R$	$X = H$	$X = V$	$X = R$	$X = H$
5151	4316	4763	630	533	582

temperature of WO_3 by equations (3.9) and (3.10). The relationship between the Debye temperature and the average wave velocity is as follows:

$$\upsilon_s = \sqrt{\frac{G_x}{\rho}}; \upsilon_p = \sqrt{\frac{B_x + 4G_x/3}{\rho}}; \upsilon_m = \left(\frac{2/\upsilon_s{}^3 + 1/\upsilon_p{}^3}{3}\right)^{-1/3} \tag{3.9}$$

and

$$\Theta = \frac{h}{k}\left(\frac{3nN_A\rho}{4\pi M}\right)^{1/3} \upsilon_m, \tag{3.10}$$

where h is the Planck constant, k is the Boltzmann constant, N_A is the Avogadro constant, M is the molecular weight and ρ is the density (table 3).

The Debye temperature is calculated to be 582 K; unfortunately, there are no data available for comparison in the literature, as far as we know. To analyse the results, we only compared other functional materials, such as GaN (390), ZnO (303) and Al_2O_3(370) [61,62]; it can be found that WO_3 has a higher Debye temperature, which shows that the interatomic binding force, melting point, hardness and thermal expansion coefficient of WO_3 are larger than those of the above materials.

3.4. Anisotropy of elastic wave velocity

For cubic WO_3, the propagation velocity of longitudinal and transverse waves along different crystal directions is related to the elastic constants C_{ij}. In table 4, the equations relating velocities of propagation and elastic constants used for the calculations on WO_3 are given.

From table 4, we can draw a conclusion: for cubic WO_3, v_1 is the largest of longitudinal wave velocities; the wave is a pure longitudinal wave in the direction of [100], while in [110] and [111], waves of v_3 and v_6 are quasi-longitudinal waves. In a pure longitudinal wave, the direction of the particle vibration is perpendicular to the forward direction of the wave, whereas for the quasi-longitudinal wave it is not so, and the velocity component will be produced in other directions, and therefore $v_1 > v_3, v_6$. The velocities for v_3, v_4 and v_5 are all different; transverse waves, which are formed by the degeneracy split into v_4 and v_5, have different velocities. Based on the above-mentioned reasons, we can conclude that it is anisotropy in this direction.

Table 4. Relation of velocity to elastic constants for various modes of propagation.

orientation of WO_3 sample	mode of propagation	relation of velocity to elastic constants	calculated velocity
[100]	longitudinal	$v_1 = \sqrt{C_{11}/\rho}$	9040
[100]	transverse	$v_2 = \sqrt{C_{44}/\rho}$	3260
[110]	longitudinal	$v_3 = \sqrt{(C_{11} + C_{12} + 2C_{44})/2\rho}$	7356
[110]	transverse	$v_4 = \sqrt{C_{44}/\rho}$	3260
[110]	transverse	$v_5 = \sqrt{(C_{11} - C_{12})/2\rho}$	6184
[111]	longitudinal	$v_6 = \sqrt{(C_{11} + 2C_{12} + 4C_{44})/3\rho}$	6701
[111]	transverse	$v_7 = \sqrt{(C_{11} - C_{12} + C_{44})/3\rho}$	5389

4. Conclusion

In this paper, we have performed first-principles calculations on cubic WO_3, including structural parameters as well as the band structure, density of state, elastic constants, Debye temperature and the acoustic wave velocity in different directions. The calculated results show that the cubic WO_3 is an indirect band-gap oxide; the valence band is mainly composed of O-2p, and the bottom of the conduction band is mainly contributed by W-5d and a few of O-2p. There is no doubt about the importance of elastic constants in this work; based on the elastic constants, the bulk, shear and Young's modulus are also further studied, which shows that the shear modulus is determined according to the stability of cubic WO_3. Vickers' hardness and Poisson ratio are also investigated by obtaining the bulk and the shear modulus; there is no research on the hardness of WO_3, and we can only compare it with other oxides.

The calculation of Debye temperature is further obtained by elastic constants, as 582 K, which is useful not only for the potential application of WO_3 on thermoelectric and thermal resistance materials but also for the development of thermoelectric materials in future. Finally, we investigated the acoustic wave velocities in different directions. Based on the concept of pure and quasi wave, and the calculated result of wave velocity, it can be shown that cubic WO_3 acoustic waves have anisotropy in the [110] direction.

Data accessibility. The datasets supporting this article have been uploaded as part of the electronic supplementary material.

Authors' contributions. L.X. carried out all simulations and wrote the first draft of the manuscript under the supervision of H.-Q.F. The manuscript correction and revision have been carried out by both authors.

Competing interests. We declare we have no competing interests.

Funding. This work was supported by the National Natural Science Foundation (51672220) and 111 Program (B08040) of MOE, the National Defense Science Foundation (32102060303), the Xi'an Science and Technology Foundation, the Shaanxi Provincial Science Foundation and NPU Gaofeng Project (17GH020824) of China.

References

1. Qi C, Bao W, Wang L, Li H, Wu W. 2017 Study of the V_2O_5-WO_3/TIO_2 catalyst synthesized from waste catalyst on selective catalytic reduction of NO_x by NH_3. *Catalysts* **7**, 110. (doi:10.3390/catal7040110)
2. Alaya MN, Rabah MA. 2017 Some physico-chemical properties and catalytic activity of sulfate ion supported on WO_3 /SnO_2, catalyst . *Arab. J. Chem.* **10**, S439–S449. (doi:10.1016/j.arabjc.2012.10.004)
3. Chen Y *et al.* 2017 Tuning electronic states of catalytic sites enhances SCR activity of hexagonal WO_3 by Mo framework substitution. *Catal. Sci. Technol.* **7**, 2467–2473. (doi:10.1039/C7CY00416H)
4. Bin JK, Na YL, Lee SJ, Seo B, Yang J, Kim J, Yoon SY, Kang I. 2016 Two stacked tandem white organic light-emitting diodes employing WO_3 as a charge generation layer. *Proc. SPIE* **9941**, 99411T. (doi:10.1117/12.2236438)
5. Dirany N, Arab M, Madigou V, Leroux C, Gavarri JR. 2017 A facile one step route to synthesize WO_3 nanoplatelets for CO oxidation and photodegradation of RhB: microstructural, optical and electrical studies. *Rsc Adv.* **6**, 69 615–69 626. (doi:10.1039/C6RA13500E)
6. Xin Y, Wang G, Zhu X, Gao M, Liu Y, Chen Q. 2017 Photodegradation performance and mechanism of 4-nonylphenol by WO_3/TiO_2 and TiO_2 nanotube array photoelectrodes. *Environ. Technol.* **38**, 3084–3092. (doi:10.1080/09593330.2017.1290143)
7. Momeni MM, Ghayeb Y. 2015 Photochemical deposition of platinum on titanium dioxide–tungsten trioxide nanocomposites: an efficient photocatalyst under visible light irradiation. *J. Mater. Sci. Mater. Electron.* **27**, 1–8. (doi:10.1007/s10854-015-3852-z)
8. Wang S, Lan Z, Huang Y. 2016 Flame aerosol synthesis of tungsten trioxide powder: particle morphology control and photodegradation activity under visible light irradiation. *Powder Technol.* **294**, 259–265. (doi:10.1016/j.powtec.2016.02.043)
9. Deb SK. 2008 Opportunities and challenges in science and technology of WO_3, for electrochromic and related applications . *Sol. Energy Mater. Sol. Cells* **92**, 245–258. (doi:10.1016/j.solmat.2007.01.026)
10. Simchi H, Mccandless BE, Meng T, Shafarman WN. 2014 Structural, optical, and surface properties of WO_3, thin films for solar cells. *J. Alloys Compd.* **617**, 609–615. (doi:10.1016/j.jallcom.2014.08.047)
11. Randin JP. 1978 Chemical and electrochemical stability of WO_3, electrochromic films in liquid electrolytes. *J. Electron. Mater.* **7**, 47–63. (doi:10.1007/BF02656020)

12. Chen D, Ye J. 2010 Hierarchical WO_3 hollow shells: dendrite, sphere, dumbbell, and their photocatalytic properties. *Adv. Funct. Mater.* **18**, 1922–1928. (doi:10.1002/adfm.200701468)
13. Rahimnejad S, He JH, Pan F, Lee X, Chen W, Wu K, Qin Xu G. 2014 Enhancement of the photocatalytic efficiency of WO_3 nanoparticles via hydrogen plasma treatment. *Mater. Res. Express* **1**, 045044. (doi:10.1088/2053-1591/1/4/045044)
14. Garcia-Belmonte G, Bueno PR, Fabregat-Santiago F, Bisquert J. 2004 Relaxation processes in the coloration of amorphous WO_3 thin films studied by combined impedance and electro-optical measurements. *J. Appl. Phys.* **96**, 853–859. (doi:10.1063/1.1759083)
15. García-Cañadas J, Mora-Seró I, Fabregat-Santiago F, Bisquert J, Garcia-Belmonte G. 2004 Analysis of cyclic voltammograms of electrochromic α -WO_3, films from voltage-dependent equilibrium capacitance measurements. *J. Electroanal. Chem.* **565**, 329–334. (doi:10.1016/j.jelechem.2003.10.027)
16. Sadek AZ *et al.* 2009 High-temperature anodized WO_3 nanoplatelet films for photosensitive devices. *Langmuir* **25**, 9545–9551. (doi:10.1021/la901944x)
17. Deb S, Aditya S. 2004 Preparation of photosensitive WO_3 sol, its use in photocatalysis, photogalvanic cell and feasibility of fuel cell at room temperature. *J. Indian Chem. Soc.* **81**, 1163–1166.
18. Ren Y, Gao Y, Zhao G. 2015 Facile single-step fabrications of electrochromic WO_3, micro-patterned films using the novel photosensitive sol–gel method. *Ceram. Int.* **41**, 403–408. (doi:10.1016/j.ceramint.2014.08.084)
19. Teoh LG, Hon YM, Shieh J, Lai WH, Hon MH. 2003 Sensitivity properties of a novel NO_2, gas sensor based on mesoporous WO_3, thin film. *Sens. Actuators B Chem.* **96**, 219–225. (doi:10.1016/S0925-4005(03)00528-8)
20. Penza M, Vasanelli L. 1997 SAW NO_x gas sensor using WO_3 thin-film sensitive coating. *Sens. Actuators B Chem.* **41**, 31–36. (doi:10.1016/S0925-4005(97)80274-2)
21. Hieu NV, Quang VV, Hoa ND, Kim D. 2011 Preparing large-scale WO_3 nanowire-like structure for high sensitivity NH gas sensor through a simple route. *Curr. Appl. Phys.* **11**, 657–661. (doi:10.1016/j.cap.2010.11.002)
22. Yan J, Wang T, Wu G, Dai W, Guan N, Li L, Gong J. 2015 Tungsten oxide single crystal nanosheets for enhanced multichannel solar light harvesting. *Adv. Mater.* **27**, 1580–1586. (doi:10.1002/adma.201404792)
23. Hsieh YT, Huang MW, Chang CC, Chen U-S, Shih H-C. 2010 Growth and optical properties of uniform tungsten oxide nanowire bundles via a two-step heating process by thermal evaporation. *Thin Solid Films* **519**, 1668–1672. (doi:10.1016/j.tsf.2010.08.162)
24. Hao Lai W, Shieh J, Gaik Teoh L, Hon MH. 2005 Fabrication of one-dimensional mesoporous tungsten oxide. *Nanotechnology* **17**, 110. (doi:10.1088/0957-4484/17/1/018)
25. Wang F, Valentin CD, Pacchioni G. 2011 Electronic and structural properties of WO_3: a systematic hybrid DFT study. *J. Phys. Chem. C* **115**, 8345–8353. (doi:10.1021/jp201057m)
26. Levy M, Pagnier T. 2007 Ab initio DFT computation of SnO_2, and WO_3, slabs and gas–surface interactions. *Sens. Actuators B Chem.* **126**, 204–208. (doi:10.1016/j.snb.2006.11.047)
27. Chatten R, Chadwick AV, Rougier A, Lindan PJ. 2005 The oxygen vacancy in crystal phases of WO_3. *J. Phys. Chem. B* **109**, 3146. (doi:10.1021/jp045655r)
28. Lowther JE. 2005 Compressibility of highly coordinated metal oxynitrides: LDA calculations. *Phys. Rev. B* **72**, 2105. (doi:10.1103/PhysRevB.72.172105)
29. Kraetschmer W, Buettgen N, Loidl A, Scheidt EW. 2009 Intermediate-valence behavior in the transition-metal oxide $CaCu_3Ru_4O_{12}$. *APS Meeting Abstracts*.
30. Wang QB, Zhou C, Chen L, Wang X-C, He K-H. 2014 The optical properties of NiAs phase ZnO under pressure calculated by GGA+ U, method. *Opt. Commun.* **312**, 185–191. (doi:10.1016/j.optcom.2013.09.035)
31. Morgan BJ, Watson GW. 2010 Intrinsic n-type defect formation in TiO_2: a comparison of rutile and anatase from GGA + U calculations. *J. Phys. Chem. C* **114**, 2321. (doi:10.1021/jp9088047)
32. Morgan BJ, Madden PA. 2012 Lithium intercalation into TiO_2(B): a comparison of LDA, GGA, and GGA + U density functional calculations. *Phys. Rev. B Condens. Matter* **86**, 6335.
33. Ao B, Zhang Z, Tang T, Zhao Y. 2015 Roles of Cu concentration in the photocatalytic activities of Cu-doped TiO_2 from GGA + U calculations. *Solid State Commun.* **204**, 23–27. (doi:10.1016/j.ssc.2014.12.006)
34. Finazzi E, Di VC, Pacchioni G, Selloni A. 2008 Excess electron states in reduced bulk anatase TiO_2: comparison of standard GGA, GGA + U, and hybrid DFT calculations. *J. Chem. Phys.* **129**, 035108. (doi:10.1063/1.2996362)
35. Loschen C, Carrasco J, Neyman KM, Illas F. 2007 First-principles LDA + U, and GGA + U, study of cerium oxides: dependence on the effective U parameter. *Phys. Rev. B* **75**, 5115. (doi:10.1103/PhysRevB.75.035115)
36. Clark SJ, Segall MD, Pickard CJ, Hasnip PJ, Probert MI, Refson K, Payne MC. 2005 First principles methods using CASTEP. *Z. Kristallogr.* **220**, 567–570.
37. Malik R, Franke L, Siebes A. 2001 Calculation of electronic energy and density of state of iron-disilicides using a total-energy pseudopotential method, CASTEP. *Thin Solid Films* **381**, 176–182. (doi:10.1016/S0040-6090(00)01740-5)
38. Lichtenstein A. 1999 First-principles calculations of electronic structure and spectra of strongly correlated systems: the LDA + U method. *J. Phys. Condens. Matter* **9**, 7359–7367.
39. Christensen NE, Mackintosh AR. 1987 Electronic structure of cubic sodium tungsten bronze. *Phys. Rev. B Condens. Matter* **35**, 8246–8248. (doi:10.1103/PhysRevB.35.8246)
40. Hjelm A, Granqvist CG, Wills JM. 1996 Electronic structure and optical properties of WO_3, $LiWO_3$, Na WO_3, and HWO_3. *Phys. Rev. B* **54**, 2436. (doi:10.1103/PhysRevB.54.2436)
41. Cora F, Patel A, Harrison NM, Dovesi R, Catlow CR. 1996 An ab initio Hartree-Fock study of the cubic and tetragonal phases of bulk tungsten trioxide. *J. Am. Chem. Soc* **118**, 12 174–12 182. (doi:10.1021/ja961514u)
42. Balázsi C, Farkas-Jahnke M, Kotsis I, Petrás L, Pfeifer J. 2001 The observation of cubic tungsten trioxide at high-temperature dehydration of tungstic acid hydrate. *Solid State Ion.* **141–142**, 411–416. (doi:10.1016/S0167-2738(01)00806-2)
43. Detraux F, Ghosez P, Gonze X. 1997 Anomalously large Born effective charges in cubic WO_3. *Phys. Rev. B* **56**, 983–985. (doi:10.1103/PhysRevB.56.983)
44. Wijs GAD, Boer PKD, Groot RAD, Kresse G. 1999 Anomalous behavior of the semiconducting gap in W03, from first-principles calculations. *Phys. Rev. B* **59**, 2684–2693. (doi:10.1103/PhysRevB.59.2684)
45. Koffyberg FP, Dwight K, Wold A. 1979 Interband transitions of semiconducting oxides determined from photoelectrolysis spectra. *Solid State Commun.* **30**, 433–437. (doi:10.1016/0038-1098(79)91182-7)
46. Fiorentini VV, Baldereschi A. 1995 Dielectric scaling of the self-energy scissor operator in semiconductors and insulators. *Phys. Rev. B: Condens. Matter* **51**, 17 196–17 198. (doi:10.1103/PhysRevB.51.17196)
47. Born M, Huang K, Lax M. 1954 Dynamical theory of crystal lattices. *Am. J. Phys.* **39**, 113–127.
48. Reuss AZ. 2006 Berechnung der Fliessgrenze von Mischkristallen auf Grund der Plastizitätsbedingung für Einkristalle. *Z. Angew. Math. Mech.* **9**, 49–58. Zamm Journal of Applied Mathematics & Mechanics, 2006;9(1):49–58. (doi:10.1002/zamm.19290090104)
49. Voigt W. 1928 *Lehrbuch der Kristallphysik*. B.G. Teubner.
50. Hill R. 1952 The elastic behaviour of a crystalline aggregate. *Proc. Phys. Soc.* **65**, 349–354. (doi:10.1088/0370-1298/65/5/307)
51. Dendzik Z, Chrobak D, Nowak R. 2009 Elastic constants and analytic bond order potential for atomistic simulations of simple cubic tungsten trioxide. *Task Q. Sci. Bull. Acad. Comput. Cent. Gdansk* **30**, 1751–1760.
52. Cora F, Stachiotti MG, Catlow CRA, Rodriguez CO. 2010 ChemInform abstract: transition metal oxide chemistry: electronic structure study of WO_3, ReO_3, and $NaWO_3$. *Cheminform* **28**, 3945–3952.
53. Pagnier T, Pasturel A. 2003 An ab initio study of WO_3 under pressure up to 30 GPa. *J. Phys. Condens. Matter* **15**, 3121–3133. (doi:10.1088/0953-8984/15/19/313)
54. Cheong FC, Varghese B, Zhu Y, Tan EP, Dai L, Tan VB, Lim CT, Sow CH. 2007 WO_{3-x} nanorods synthesized on a thermal hot plate. *J. Phys. Chem. C* **111**, 17 193–17 199. (doi:10.1021/jp074569z)
55. Pugh S. 2009 FXCII. Relations between the elastic moduli and the plastic properties of polycrystalline pure metals. *Philos. Mag.* **45**, 823–843.
56. Liu QJ, Liu ZT, Feng LP. 2011 Elasticity, electronic structure, chemical bonding and optical properties of monoclinic ZrO_2 from first-principles. *Phys. B Phys. Condens. Matter* **406**, 345–350. (doi:10.1016/j.physb.2010.10.057)
57. Liu Q, Liu Z, Feng L, Xu B. 2009 First-principles study of structural, optical and elastic properties of cubic HfO_2. *Phys. B Condens. Matter* **404**, 3614–3619. (doi:10.1016/j.physb.2009.06.061)
58. Iuga M, Steinle-Neumann G, Meinhardt J. 2007 Ab-initio simulation of elastic constants for some ceramic materials. *Eur. Phys. J. B* **58**, 127–133. (doi:10.1140/epjb/e2007-00209-1)
59. Fu J, Bernard F, Kamali-Bernard S. 2017 First-principles calculations of typical anisotropic cubic and hexagonal structures and homogenized moduli estimation based on the Y-parameter: application to CaO, MgO, CH and Calcite CaCO3. *J. Phys. Chem. Solids* **101**, 74–89. (doi:10.1016/j.jpcs.2016.10.010)

60. Tsuchiya T, Kawamura K. 2001 Systematics of elasticity: Ab initio study in B1-type alkaline earth oxides. *J. Chem. Phys.* **114**, 10 086–10 093. (doi:10.1063/1.1371498)
61. Morelli DT, Slack GA. 2006 High lattice thermal conductivity solids. In *High Thermal Conductivity materials* (eds SL Shinde, J Goela), pp. 37–68. Berlin, Germany: Springer.
62. Slack GA. 1979 The thermal conductivity of nonmetallic crystals. In *Solid State Physics, vol. 34*. (eds H Ehrenreich, F Seitz, D Turnbull), pp. 1–71. New York, NY: Academic Press.